mathematics

Article

Solution-Space-Reduction-Based Evidence Theory Method for Stiffness Evaluation of Air Springs with Epistemic Uncertainty

Shengwen Yin, Keliang Jin, Yu Bai, Wei Zhou * and Zhonggang Wang

Key Laboratory of Traffic Safety on Track, Ministry of Education, School of Traffic & Transportation Engineering, Central South University, Changsha 410075, China
* Correspondence: gszx_zhouwei@csu.edu.cn

Abstract: In the Dempster–Shafer evidence theory framework, extremum analysis, which should be repeatedly executed for uncertainty quantification (UQ), produces a heavy computational burden, particularly for a high-dimensional uncertain system with multiple joint focal elements. Although the polynomial surrogate can be used to reduce computational expenses, the size of the solution space hampers the efficiency of extremum analysis. To address this, a solution-space-reduction-based evidence theory method (SSR-ETM) is proposed in this paper. The SSR-ETM invests minimal additional time for potentially high-efficiency returns in dealing with epistemic uncertainty. In the SSR-ETM, monotonicity analysis of the polynomial surrogate over the range of evidence variables is first performed. Thereafter, the solution space can be narrowed to a smaller size to accelerate extremum analysis if the surrogate model is at least monotonic in one dimension. Four simple functions and an air spring system with epistemic uncertainty demonstrated the efficacy of the SSR-ETM, indicating an apparent superiority over the conventional method.

Keywords: solution space reduction; Dempster–Shafer evidence theory; monotonicity analysis; air spring; epistemic uncertainty; uncertainty quantification

MSC: 65D40

check for updates

Citation: Yin, S.; Jin, K.; Bai, Y.; Zhou, W.; Wang, Z. Solution-Space-Reduction-Based Evidence Theory Method for Stiffness Evaluation of Air Springs with Epistemic Uncertainty. *Mathematics* **2023**, *11*, 1214. https://doi.org/10.3390/math11051214

Academic Editors: Jin Peng and Dan Ralescu

Received: 13 January 2023
Revised: 15 February 2023
Accepted: 24 February 2023
Published: 1 March 2023

1. Introduction

Air springs are core components of the secondary suspension system of high-speed trains, whose stiffness performance is closely related to the stability and safety of train operations. The stiffness evaluation of air springs is conventionally based on deterministic approaches [1,2]. However, air springs involve inevitable uncertainties, subject to various raw materials and complex processing technologies. Their stiffness performance is more elusive under the coupling effect of the atmosphere and chronic external excitation. Given the crucial role of air springs in train operation, it is imperative to predict their stiffness performance under uncertainty.

There are two categories of uncertainty: aleatory uncertainty and epistemic uncertainty [3]. Aleatory uncertainty is attributed to the inherent variability of the system or working environment [4]. Although probability-based aleatory uncertainty is broadly researched in engineering [5–8], it is inappropriate for limited data. Epistemic uncertainty results from an incomplete or inadequate knowledge of the physical system [9]. Thus far, non-probabilistic methods such as the Dempster–Shafer evidence theory [10,11], fuzzy set theory [12–14], interval analysis [15–18], and generalised p-boxes [19,20] have been widely applied to describe epistemic uncertainty. Among the non-probabilistic methods mentioned above, the Dempster–Shafer evidence theory supports a relatively flexible mathematical framework equivalent to interval analysis or probability-based methods under particular conditions [9]. Such characteristics promote the extensive application of the Dempster–Shafer evidence theory in reliability analysis and response analysis [21–23].

Recently, polynomial chaos expansion (PCE) [24–27], which approximates computational models through a linear combination of orthogonal polynomials, has been introduced to the Dempster–Shafer evidence theory framework for UQ. Harsheel et al. [28] introduced the Legendre polynomial surrogate to address engineering problems with hybrid uncertainties. Subsequently, Yin et al. [9,29] employed a Jacobi polynomial surrogate and an arbitrary PCE for the response analysis of acoustic systems with epistemic uncertainty. However, the required number of model evaluations for a PCE increases significantly with the size of the uncertain vector; this is also known as the 'curse of dimensionality'. Consequently, sparse PCE [30–33], which uses the sparsity-of-effects principle and powerful sparse regression solvers to approximate high-dimensional computational models through a few model evaluations, has been used [34].

Although sparse PCE provides an inexpensive approximation to the computational model, the efficiency of extremum analysis is limited to the size of the solution space. In particular, extremum analysis must be executed in each joint focal element for an evidence-theory-based UQ. Many engineering problems involve a large number of uncertain parameters, and the interval of the uncertain parameters is usually divided into as many focal elements as possible to improve the reliability of UQ. The calculation time of the conventional method [9,29] carrying out extremum analysis in the original solution space is unacceptable. To narrow the size of the solution space, SSR-ETM, which takes advantage of the monotonicity of the PCE-based surrogate model, is proposed. The monotonicity over the range of evidence variables is available for all joint focal elements. If the surrogate model is at least monotonic in one dimension, the size of the solution spaces can be reduced to increase the computational efficiency.

The contributions of this paper are as follows: (1) the Dempster–Shafer evidence theory was employed to quantify epistemic uncertainty; (2) the sparse PCE was introduced to construct the surrogate model, and the input variables with arbitrary probability measures were considered; (3) a method, namely SSR-ETM, was proposed to accelerate evidence-theory-based UQ; (4) different types of numerical examples are designed to discuss the shortcomings and advantages of SSR-ETM, and good results are obtained in an air spring system with epistemic uncertainty.

The remainder of this paper is organised as follows. Section 2 presents the theoretical framework of the Dempster–Shafer evidence theory. Section 3 introduces the SSR-ETM framework and its core steps. In Section 4, four simple functions and an air spring system with epistemic uncertainty are used to verify the superiority of the SSR-ETM. Section 5 presents the concluding remarks.

2. Fundamentals of the Dempster–Shafer Evidence Theory

The Dempster–Shafer evidence theory, abbreviated as evidence theory, owes its name to the pioneering work by Dempster [35] and Shafer [36–38]; it is a generalisation of the Bayesian theory of subjective probability [39]. In evidence theory, the frame of discernment (FD) Θ is defined as a finite exhaustive set of w pairwise mutually exclusive propositions as follows:

$$\Theta = \{h_1, h_2, \ldots, h_w\}. \tag{1}$$

where $h_1, h_2, \ldots, h_w$ are the elementary propositions.

The combination of all subsets of Θ constitutes a power set 2^Θ that contains the following possible propositions:

$$2^\Theta = \{\varnothing, \{h_1\}, \{h_2\}, \ldots, \{h_w\}, \{h_1, h_2\}, \{h_1, h_3\}, \ldots, \{h_{w-1}, h_w\}, \ldots, \Theta\}. \tag{2}$$

Basic probability assignment (BPA), an independent probability-like measure, is assigned to each possible proposition to indicate belief information [40]. The BPA $m(A)$ of the subset A is

$$\begin{cases} m(A) \geq 0, \forall A \in 2^\Theta, \\ m(\varnothing) = 0, \\ \sum\limits_{A \in 2^\Theta} m(A) = 1, \end{cases} \tag{3}$$

where A is defined as the focal element once $m(A) > 0$.

The evidence theory model is an uncertainty model based on evidence theory that converts the uncertain vector $\boldsymbol{x} = [x_1, x_2, \ldots, x_d]$ into an evidence vector $\boldsymbol{\xi} = [\xi_1, \xi_2, \ldots, \xi_d]$ composed of d independent evidence variables. A multi-index set $\boldsymbol{\kappa}$ that contains all index combinations of the focal element is defined as

$$\boldsymbol{\kappa} = \left\{ \boldsymbol{\beta} \in \mathbb{N}_+^d : \beta_i \leq N_i, i = 1, 2, \ldots, d \right\} \text{ with } \mathrm{card}(\boldsymbol{\kappa}) = N_f = \prod_{i=1}^{d} N_i, \tag{4}$$

where $\mathbb{N}_+$ is the set of positive integers, N_i is the number of focal elements of ξ_i, and $\boldsymbol{\beta}$ is a multi-index. The joint focal element $\varepsilon_{\boldsymbol{\beta}}$, which can be regarded as a solution space, is spanned by focal elements, given by

$$\varepsilon_{\boldsymbol{\beta}} = \varepsilon_{\beta_1} \times \varepsilon_{\beta_2} \ldots \times \varepsilon_{\beta_d} \tag{5}$$

where $\varepsilon_{\beta_i} = [\underline{\varepsilon}_{\beta_i}, \overline{\varepsilon}_{\beta_i}]$ is the β_i-th focal element of ξ_i. The BPA of $\varepsilon_{\boldsymbol{\beta}}$, denoted by $m(\varepsilon_{\boldsymbol{\beta}})$, is defined as the product of the BPAs of focal elements, as follows:

$$m(\varepsilon_{\boldsymbol{\beta}}) = \prod_{i=1}^{d} m(\varepsilon_{\beta_i}) \tag{6}$$

In the evidence theory model, the lower and upper bounds of the true extent of a proposition B, belief (Bel) and plausibility (Pl), are defined as

$$\mathrm{Bel}(B) = \sum_{A \subseteq B} m(A), \tag{7}$$

$$\mathrm{Pl}(B) = \sum_{A \cap B = \varnothing} m(A), \tag{8}$$

Based on Bel and Pl, the cumulative belief function (CBF) and cumulative plausibility function (CPF) of system response are defined as

$$\mathrm{CBF}(u) = \mathrm{Bel}(y(\boldsymbol{\xi}) \leq u) = \sum_{\{\varepsilon_{\boldsymbol{\beta}} | \overline{y}_{\boldsymbol{\beta}} \leq u, \boldsymbol{\beta} \in \boldsymbol{\kappa}\}} m(\varepsilon_{\boldsymbol{\beta}}), \tag{9}$$

$$\mathrm{CPF}(u) = \mathrm{Pl}(y(\boldsymbol{\xi}) \leq u) = \sum_{\{\varepsilon_{\boldsymbol{\beta}} | \underline{y}_{\boldsymbol{\beta}} \leq u, \boldsymbol{\beta} \in \boldsymbol{\kappa}\}} m(\varepsilon_{\boldsymbol{\beta}}), \tag{10}$$

where $\underline{y}_{\boldsymbol{\beta}}$ and $\overline{y}_{\boldsymbol{\beta}}$ are the minimum and maximum values, respectively, of the system response in $\varepsilon_{\boldsymbol{\beta}}$, with u is a constant. As the lower and upper boundaries of the cumulative distribution functions (CDFs), CBF and CPF enclose the real CDF of the system response.

Other statistical properties, such as the system response expectation and variance, can be obtained. Owing to the uncertain probability distributions of the evidence variables, the expectation and variance of the system response, denoted by μ^{I} and $\mathrm{var}^{\mathrm{I}}$, are expressed in the following variation ranges [41]:

$$\mu^{\mathrm{I}} = \sum_{\boldsymbol{\beta} \in \boldsymbol{\kappa}} y_{\boldsymbol{\beta}}^{\mathrm{I}} m(\varepsilon_{\boldsymbol{\beta}}), \tag{11}$$

$$\mathrm{var}^{\mathrm{I}} = \sum_{\boldsymbol{\beta} \in \boldsymbol{\kappa}} \left(y_{\boldsymbol{\beta}}^{\mathrm{I}} - \mu^{\mathrm{I}} \right)^2 m(\varepsilon_{\boldsymbol{\beta}}), \tag{12}$$

where $y_{\boldsymbol{\beta}}^{\mathrm{I}} = [\underline{y}_{\boldsymbol{\beta}}, \overline{y}_{\boldsymbol{\beta}}]$ is the response interval determined via extremum analysis, which is essentially equivalent to solving the following optimisation problem:

$$\begin{aligned} &\underline{y}_{\boldsymbol{\beta}} = \min y_{\boldsymbol{\beta}} \text{ or } \overline{y}_{\boldsymbol{\beta}} = \max y_{\boldsymbol{\beta}} \\ &s.t.\ \boldsymbol{\xi}_{\boldsymbol{\beta}} \in \varepsilon_{\boldsymbol{\beta}}, \boldsymbol{\beta} \in \boldsymbol{\kappa}. \end{aligned} \tag{13}$$

3. SSR-ETM for Evidence-Theory-Based UQ

3.1. Framework of the SSR-ETM

In high-dimensional engineering applications, extremum analysis requires a large amount of computation. The size of the solution space is one of the main factors. Thus, SSR-ETM is proposed to mitigate the restriction of the size of solution space on efficiency under the precondition that the surrogate model is monotonic in one or more dimensions. As shown in Figure 1, the domain consists of solution spaces. In the SSR-ETM, the three-dimensional original solution space shown in Figure 1 can be reduced to a low-dimensional solution space. Depending on the number of monotonic dimensions, the reduced solution space may be a two-dimensional plane, line segment, or point.

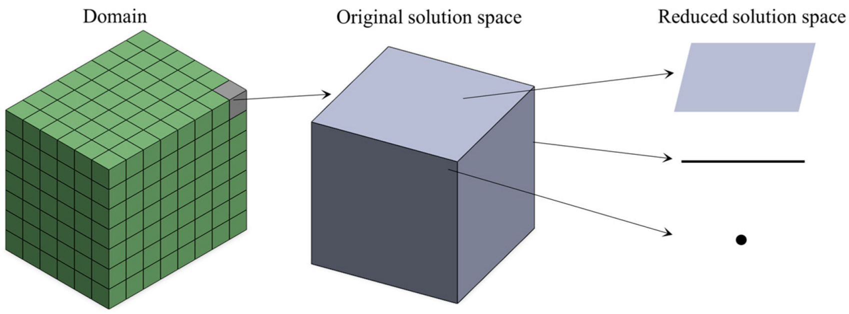

Figure 1. Domain, original solution space, and its reduced solution spaces.

The framework of the SSR-ETM is shown in Figure 2, which also presents the framework of the conventional methods in [9,29], collectively known as the evidence theory method (ETM) here, for a clear comparison. The grey parts, the blue part, and the red part are performed in the domain, reduced solution spaces, and original solution spaces, respectively. In the SSR-ETM, monotonicity analysis is performed only once, and the extremum analysis must be executed N_f times.

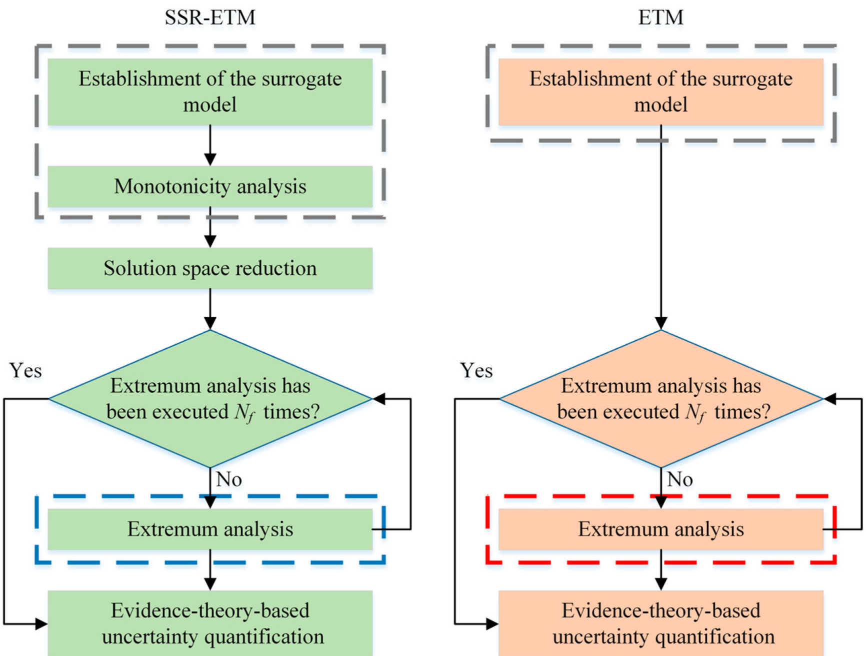

Figure 2. Framework of the SSR-ETM and ETM.

3.2. Establishment of Sparse Representation

Suppose $\boldsymbol{x} = [x_1, x_2, \ldots, x_d] \in \mathbb{R}^d$ is a d-dimensional random vector in a continuous domain Ω, with each random variable being independent. Accordingly, the computational model $y(\boldsymbol{x})$ can be expressed using PCE as follows:

$$y(\boldsymbol{x}) \approx \sum_{\boldsymbol{\alpha} \in \hat{\lambda}} f_{\boldsymbol{\alpha}} \psi_{\boldsymbol{\alpha}}(\boldsymbol{x}), \tag{14}$$

where $\boldsymbol{\alpha} = [\alpha_1, \alpha_2, \ldots, \alpha_d] \in \hat{\lambda}$ is a multi-index indicating the orders of multivariate orthogonal polynomials $\left\{\psi_{\boldsymbol{\alpha}}(\boldsymbol{x}), \boldsymbol{\alpha} \in \hat{\lambda}\right\}$, $\hat{\lambda}$ is a multi-index set, and $\left\{f_{\boldsymbol{\alpha}}, \boldsymbol{\alpha} \in \hat{\lambda}\right\}$ are multivariate orthogonal polynomial coefficients [42]. PCE is usually truncated to a finite number of terms. The total order expansion technique [43] employed here yields an updated multi-index set $\hat{\lambda}_{d,\tau}$, as follows:

$$\hat{\lambda}_{d,\tau} = \left\{\boldsymbol{\alpha} \in \mathbb{N}^d : |\boldsymbol{\alpha}| \leq \tau\right\} = \{\boldsymbol{\alpha}^{(1)}, \ldots, \boldsymbol{\alpha}^{(P)}\} \text{ with } \operatorname{card}\left(\hat{\lambda}_{d,\tau}\right) \equiv P = \frac{(\tau + d)!}{\tau! d!}. \tag{15}$$

$\psi_{\boldsymbol{\alpha}}(\boldsymbol{x})$ is defined as the tensor product of univariate orthogonal polynomials, i.e.,

$$\psi_{\boldsymbol{\alpha}}(\boldsymbol{x}) = \prod_{i=1}^{d} \psi_{\alpha_i}(x_i), \tag{16}$$

where $\psi_{\alpha_i}(x_i)$ is a α_i-order univariate orthogonal polynomial related to the probability density function (PDF) $\rho(x_i)$. In addition, $\psi_{\boldsymbol{\alpha}}(\boldsymbol{x})$ satisfies orthogonality:

$$\int_{\Omega} \psi_{\boldsymbol{\alpha}_1}(\boldsymbol{x}) \psi_{\boldsymbol{\alpha}_2}(\boldsymbol{x}) \rho(\boldsymbol{x}) d\boldsymbol{x} = \delta_{\boldsymbol{\alpha}_1, \boldsymbol{\alpha}_2}, \tag{17}$$

with $\delta_{\boldsymbol{\alpha}_1, \boldsymbol{\alpha}_2}$ as the Kronecker delta and $\rho(\boldsymbol{x}) = \prod_{i=1}^{d} \rho_i(x)$ as the joint PDF.

Families of orthogonal polynomials about continuous distributions including Gaussian, uniform, gamma, and beta distributions were elaborated in [44]. However, random variables are not always limited to these classical distributions. In arbitrary PCE [45], orthogonal polynomials associated with arbitrary distributions can be constructed with the raw moment of random variables. The k-th raw moment u_k of a continuous random variable is defined as

$$u_k = \int_{\Omega_i} x^k \rho(x) dx. \tag{18}$$

The coefficient to the q-th power of k-order univariate orthogonal polynomial, $\varpi_q (q = 1, 2, \ldots, k)$, is calculated by

$$\begin{bmatrix} u_0 & u_1 & \cdots & u_k \\ u_1 & u_2 & \cdots & u_{k+1} \\ \vdots & \vdots & \vdots & \vdots \\ u_{k-1} & u_k & \cdots & u_{2k-1} \\ 0 & 0 & \cdots & 1 \end{bmatrix} \begin{bmatrix} \varpi_0 \\ \varpi_1 \\ \vdots \\ \varpi_{k-1} \\ \varpi_k \end{bmatrix} = \begin{bmatrix} 0 \\ 0 \\ \vdots \\ 0 \\ 1 \end{bmatrix}. \tag{19}$$

Then, the k-order univariate orthogonal polynomial is given by

$$\psi_k(x) = \sum_{q=0}^{k} \varpi_q x^q. \tag{20}$$

However, the Vandermonde matrix may be ill-conditioned for a large value of k [46]. The alternative scheme relies on the following Hankel matrix [47]:

$$\mathbf{H} = \begin{bmatrix} u_0 & u_1 & \cdots & u_k \\ u_1 & u_2 & \cdots & u_{k+1} \\ \vdots & \vdots & \vdots & \vdots \\ u_k & u_{k+1} & \cdots & u_{2k} \end{bmatrix} \tag{21}$$

Condition $\det(\mathbf{H}) > 0$, if satisfied, supports the Cholesky decomposition of $\mathbf{H} = \mathbf{R}^{\mathrm{T}}\mathbf{R}$, with $\mathbf{R}$ being an upper triangular matrix. The matrix $\mathbf{R}$ provides information on recursive coefficients [46]

$$a_k = \frac{r_{k,k+1}}{r_{k,k}} - \frac{r_{k-1,k}}{r_{k-1,k-1}}, b_k = \frac{r_{k+1,k+1}}{r_{k,k}} \tag{22}$$

of the following recurrence formula:

$$\begin{aligned} &\psi_{-1}(x) = 0, \\ &\psi_0(x) = 1, \\ &\psi_{k+1}(x) = (x - a_k)\psi_k(x) - b_k\psi_{k-1}(x), k = 0, 1, 2, \ldots . \end{aligned} \tag{23}$$

In Equation (22), $r_{i,j}(i, j = 1, 2, \ldots)$ denotes the entry in throw i and the column j of $\mathbf{R}$, with $r_{0,0} = 1$ and $r_{0,1} = 0$. $a_0 = \mu_1$ is defined here.

For a given experimental design (ED) $\boldsymbol{X} = \left\{\boldsymbol{x}^{(1)}, \ldots, \boldsymbol{x}^{(N)}\right\}^{\mathrm{T}}$ and the corresponding model evaluations $\boldsymbol{Y} = \left\{y^{(1)}, \ldots, y^{(N)}\right\}^{\mathrm{T}}$, the least-squares approach can be used to solve the polynomial coefficients $\boldsymbol{\eta} = \left\{f_{\boldsymbol{\alpha}}, \boldsymbol{\alpha} \in \lambda_{d,\tau}\right\}^{\mathrm{T}}$ as follows [48]:

$$\boldsymbol{\eta} = \underset{\boldsymbol{\alpha} \in \lambda_{d,\tau}}{\operatorname{argmin}} \|\boldsymbol{Y} - \boldsymbol{\Phi}\boldsymbol{\eta}\|_2; \boldsymbol{\eta} = \left(\boldsymbol{\Phi}^T\boldsymbol{\Phi}\right)^{-1}\boldsymbol{\Phi}^T\boldsymbol{Y}. \tag{24}$$

In Equation (24), $\boldsymbol{\Phi} \in \mathbb{R}^{N \times P}$ is a measurement matrix with entries $\Phi_{ij} = \psi_{\boldsymbol{\alpha}^{(j)}}(\boldsymbol{x}^{(i)})$. In [34,49,50], $N \approx 2P, 3P$ is recommended for a robust and unique $\boldsymbol{\eta}$. This implies that numerous model evaluations are required for a multi-dimensional computational model with high polynomial orders. To construct a polynomial surrogate using few model evaluations, Blatman and Sudret [51] successfully applied least angle regression (LAR) to a sparse PCE to find those features with the highest impact on system response. It should be noted that the "curse of dimensionality" can be alleviated to some extent through the truncation criteria (such as the total order expansion technique mentioned above) and LAR, but it cannot be completely overcome. Referring to their work, we use sparse arbitrary polynomial chaos expansion (SAPCE) to establish sparse representations, as follows:

$$y(\boldsymbol{x}) \approx C(\boldsymbol{x}) = \sum_{\boldsymbol{\alpha} \in \lambda_{\min}} f_{\boldsymbol{\alpha}}\psi_{\boldsymbol{\alpha}}(\boldsymbol{x}). \tag{25}$$

where $\lambda_{\min}$ is a multi-index selected from $\lambda_{d,\tau}$. In SAPCE, Latin hypercube sampling [52] is used as the ED generator. Then, one can rewrite Equation (13) as follows:

$$\begin{aligned} &\underline{C}(\boldsymbol{\xi}_{\boldsymbol{\beta}})/\overline{C}(\boldsymbol{\xi}_{\boldsymbol{\beta}}) = \min/\max C(\boldsymbol{\xi}_{\boldsymbol{\beta}}) \\ &s.t.\ \boldsymbol{\xi}_{\boldsymbol{\beta}} \in \varepsilon_{\boldsymbol{\beta}}, \boldsymbol{\beta} \in \boldsymbol{\kappa}, \end{aligned} \tag{26}$$

3.3. Monotonicity Analysis

On most occasions, the optimal solution to the optimisation problem is difficult to solve analytically. Heuristic algorithms [53–55] are designed for desirable solutions within acceptable computational expenses to substitute optimal solutions. However, the efficiency of heuristic algorithms is inevitably hindered by dimensionality. Favourably, numerous surrogate models are monotonic in certain dimensions. Monotonicity analysis can be employed to simplify the optimisation problem. Let us use SAPCE to approximate a differentiable computational model whose partial derivative $\frac{\partial C(\boldsymbol{\xi})}{\partial \xi_i}(i = 1, 2, \ldots, d)$ is given as

$$\frac{\partial C(\boldsymbol{\xi})}{\partial \xi_i} = \sum_{\boldsymbol{\alpha} \in \boldsymbol{\lambda}_{\min}} f_{\boldsymbol{\alpha}} \frac{\partial \prod_{i=1}^{d} \psi_{\alpha_i}(\xi_i)}{\partial \xi_i} = \sum_{\boldsymbol{\alpha} \in \boldsymbol{\lambda}_{\min}} f_{\boldsymbol{\alpha}} \frac{\psi_{\boldsymbol{\alpha}}(\boldsymbol{\xi})}{\psi_{\alpha_t}(\xi_i)} \frac{\partial \psi_{\alpha_t}(\xi_i)}{\partial \xi_i}, \tag{27}$$

where $\frac{\partial \psi_{\alpha_t}(\xi_i)}{\partial \xi_i}$ follows the three-term recurrence:

$$\begin{aligned} &\frac{\partial \psi_0(\xi_i)}{\partial \xi_i} = 0, \\ &\frac{\partial \psi_1(\xi_i)}{\partial \xi_i} = 1, \\ &\frac{\partial \psi_{k+1}(\xi_i)}{\partial \xi_i} = \psi_k(\xi_i) + (\xi_i - a_k)\frac{\partial \psi_k(\xi_i)}{\partial \xi_i} - b_k \frac{\partial \psi_{k-1}(\xi_i)}{\partial \xi_i}, k = 1, 2, \ldots . \end{aligned} \tag{28}$$

However, the PDF of evidence variables is undetermined. In other words, only the probability assigned to each focal element is available. To construct optimal orthogonal polynomials, the authors of [29] put forward a reasonable assumption that all focal elements are assigned a uniform distribution. We employ the assumption in [29] and it yields the following PDF of evidence variables:

$$\rho(\xi_i) = \sum_{\beta_i=1}^{N_i} \frac{\delta_{\beta_i}(\xi_i) m(\varepsilon_{\beta_i})}{\bar{\varepsilon}_{\beta_i} - \underline{\varepsilon}_{\beta_i}}, i = 1, 2, \ldots, d, \tag{29}$$

where $\delta_{\beta_i}(\xi_i)$ is an indicator function, indicating $\delta_{\beta_i}(\xi_i) = 1$ if $\xi_i \in \varepsilon_{\beta_i}$, or else $\delta_{\beta_i}(\xi_i) = 0$.

PSO [53] can be used to determine whether the partial derivative satisfies

$$\min\left(\frac{\partial C(\boldsymbol{\xi})}{\partial \xi_i}\right) \geq 0 \text{ or } \max\left(\frac{\partial C(\boldsymbol{\xi})}{\partial \xi_i}\right) \leq 0 \tag{30}$$

If satisfied, then the surrogate model is an increasing or decreasing function related to ξ_i; otherwise, it is a non-monotonic function. The procedure of monotonicity analysis is shown in Algorithm 1. These three cases are mapped to $p_i = 1, 2, 3$, respectively. Therefore, the set $\vartheta = \{1, 2, \ldots, d\}$, which contains indices of the dimension, can be correspondingly split into index sets $p1 = \{i \in \vartheta | p_i = 1\}$, $p2 = \{i \in \vartheta | p_i = 2\}$, and $p3 = \{i \in \vartheta | p_i = 3\}$. Let $\boldsymbol{\xi}_{\boldsymbol{\beta}}(\Xi) \in \varepsilon_{\boldsymbol{\beta}}$ and $\boldsymbol{\xi}(\Xi) \in \Omega$ be two evidence vectors under conditions Ξ. Given $\xi_i^{(1)} \leq \xi_i^{(2)}$ and $\xi_i^{(1)}, \xi_i^{(2)} \in \Omega_i$, the monotonicity of the surrogate model makes [56,57]

$$\begin{cases} C\left(\boldsymbol{\xi}(\xi_i = \xi_i^{(1)})\right) \leq C\left(\boldsymbol{\xi}(\xi_i = \xi_i^{(2)})\right), \ p_i = 1 \\ C\left(\boldsymbol{\xi}(\xi_i = \xi_i^{(2)})\right) \geq C\left(\boldsymbol{\xi}(\xi_i = \xi_i^{(1)})\right), \ p_i = 2 \end{cases}. \tag{31}$$

Thus,

$$\begin{cases} C\left(\boldsymbol{\xi}_{\boldsymbol{\beta}}(\xi_i = \underline{\varepsilon}_{\beta_i})\right) \leq C(\boldsymbol{\xi}_{\boldsymbol{\beta}}) \leq C\left(\boldsymbol{\xi}_{\boldsymbol{\beta}}(\xi_i = \bar{\varepsilon}_{\beta_i})\right), \ p_i = 1 \\ C\left(\boldsymbol{\xi}_{\boldsymbol{\beta}}(\xi_i = \underline{\varepsilon}_{\beta_i})\right) \geq C(\boldsymbol{\xi}_{\boldsymbol{\beta}}) \geq C\left(\boldsymbol{\xi}_{\boldsymbol{\beta}}(\xi_i = \bar{\varepsilon}_{\beta_i})\right), \ p_i = 2 \end{cases}. \tag{32}$$

Algorithm 1 Monotonicity analysis

Input: Surrogate model $C(\boldsymbol{\xi})$ generated by SAPCE.
1. Calculate the partial derivatives of $C(\boldsymbol{\xi})$ using Equations (27) and (28).
2. Use PSO to calculate the extremum of partial derivatives of each dimension.
3. Assess the monotonicity of the surrogate model using Equation (30).

Output: Monotonicity of the surrogate model.

In essence, monotonicity analysis uses PSO to solve the extremum of the partial derivative of the surrogate model d times. Because the extremum calculated by PSO must not be a global extremum, it may lead to a false monotonicity judgment when the minimum or maximum of the above partial derivative is very close to zero, resulting in a large error in the subsequent calculation. Generally speaking, however, the global optimization performance of PSO has been widely verified.

3.4. Solution Space Reduction for Extremum Analysis of Joint Focal Elements

The monotonicity of the surrogate model facilitates in narrowing the solution space. Let r_1, r_2, and r_3 be the number of elements in $p1$, $p2$, and $p3$, respectively. Assume $p1$, $p2$, and $p3$ divide any vector or set into three parts. It can be deduced from Equation (32) that

$$\begin{cases} C\Big(\boldsymbol{\xi}_{\boldsymbol{\beta}}(\boldsymbol{\xi}_{\boldsymbol{\beta}_{p1}} = \underline{\varepsilon}_{\boldsymbol{\beta}_{p1}})\Big) \leq C(\boldsymbol{\xi}_{\boldsymbol{\beta}}) \leq C\Big(\boldsymbol{\xi}_{\boldsymbol{\beta}}(\boldsymbol{\xi}_{\boldsymbol{\beta}_{p1}} = \overline{\varepsilon}_{\boldsymbol{\beta}_{p1}})\Big), \\ C\Big(\boldsymbol{\xi}_{\boldsymbol{\beta}}(\boldsymbol{\xi}_{\boldsymbol{\beta}_{p2}} = \underline{\varepsilon}_{\boldsymbol{\beta}_{p2}})\Big) \geq C(\boldsymbol{\xi}_{\boldsymbol{\beta}}) \geq C\Big(\boldsymbol{\xi}_{\boldsymbol{\beta}}(\boldsymbol{\xi}_{\boldsymbol{\beta}_{p2}} = \overline{\varepsilon}_{\boldsymbol{\beta}_{p2}})\Big), \end{cases} \tag{33}$$

where $\boldsymbol{\xi}_{\boldsymbol{\beta}}(\boldsymbol{\xi}_{\boldsymbol{\beta}_{p1}} = \underline{\varepsilon}_{\boldsymbol{\beta}_{p1}})$, as an example, represents

$$\boldsymbol{\xi}_{\boldsymbol{\beta}}(\boldsymbol{\xi}_{\boldsymbol{\beta}_{p1}} = \underline{\varepsilon}_{\boldsymbol{\beta}_{p1}}) = \boldsymbol{\xi}_{\boldsymbol{\beta}}(\xi_{\beta_{p1(1)}} = \underline{\varepsilon}_{\beta_{p1(1)}}, \xi_{\beta_{p1(2)}} = \underline{\varepsilon}_{\beta_{p1(2)}}, \ldots, \xi_{\beta_{p1(r_1)}} = \underline{\varepsilon}_{\beta_{p1(r_1)}}) \tag{34}$$

with $\beta_{p1(r_1)}$ being the r_1-th index of $\boldsymbol{\beta}_{p1}$. The combination of the two inequalities in Equation (33) yields

$$C\Big(\boldsymbol{\xi}_{\boldsymbol{\beta}}(\xi_{\boldsymbol{\beta}_{p1}} = \underline{\varepsilon}_{\boldsymbol{\beta}_{p1}}, \xi_{\boldsymbol{\beta}_{p2}} = \overline{\varepsilon}_{\boldsymbol{\beta}_{p2}})\Big) \leq C(\boldsymbol{\xi}_{\boldsymbol{\beta}}) \leq C\Big(\boldsymbol{\xi}_{\boldsymbol{\beta}}(\xi_{\boldsymbol{\beta}_{p1}} = \overline{\varepsilon}_{\boldsymbol{\beta}_{p1}}, \xi_{\boldsymbol{\beta}_{p2}} = \underline{\varepsilon}_{\boldsymbol{\beta}_{p2}})\Big). \tag{35}$$

Equation (35) indicates that the extremums of the optimization problems are located in the following reduced solution spaces:

$$\begin{cases} \varepsilon_{\boldsymbol{\beta}}^{\min} = \underline{\varepsilon}_{\boldsymbol{\beta}_{p1}} \times \overline{\varepsilon}_{\boldsymbol{\beta}_{p2}} \times \varepsilon_{\boldsymbol{\beta}_{p3}}, \\ \varepsilon_{\boldsymbol{\beta}}^{\max} = \overline{\varepsilon}_{\boldsymbol{\beta}_{p1}} \times \underline{\varepsilon}_{\boldsymbol{\beta}_{p2}} \times \varepsilon_{\boldsymbol{\beta}_{p3}}, \end{cases} \tag{36}$$

where $\varepsilon_{\boldsymbol{\beta}}^{\min}$ and $\varepsilon_{\boldsymbol{\beta}}^{\max}$ denote the reduced solution spaces corresponding to the minimisation/maximisation problem, respectively. The evidence vectors $\boldsymbol{\xi}_{\boldsymbol{\beta}}^{\min}$ and $\boldsymbol{\xi}_{\boldsymbol{\beta}}^{\max}$ generated in $\varepsilon_{\boldsymbol{\beta}}^{\min}$ and $\varepsilon_{\boldsymbol{\beta}}^{\max}$, respectively, are expressed as

$$\boldsymbol{\xi}_{\boldsymbol{\beta}}^{\min}/\boldsymbol{\xi}_{\boldsymbol{\beta}}^{\max} = [\xi_{\beta_1}, \xi_{\beta_2}, \ldots, \xi_{\beta_d}], \text{ where } \xi_{\beta_i}(i = 1,2,\ldots,d) = \begin{cases} \underline{\varepsilon}_{\beta_i}/\overline{\varepsilon}_{\beta_i}, \ p_i = 1 \\ \overline{\varepsilon}_{\beta_i}/\underline{\varepsilon}_{\beta_i}, p_i = 2 \\ \xi_{\beta_i} \in \varepsilon_{\beta_i}, \ p_i = 3 \end{cases}. \tag{37}$$

For instance, provided that a four-dimensional surrogate model is increasing in the first and fourth dimensions, decreasing in the second dimension, and non-monotonic in the third dimension, then, based on Equation (36), the original solution space $\varepsilon_{\boldsymbol{\beta}}$ is reduced to $\varepsilon_{\boldsymbol{\beta}}^{\min} = \underline{\varepsilon}_{\beta_1} \times \overline{\varepsilon}_{\beta_2} \times \varepsilon_{\beta_3} \times \underline{\varepsilon}_{\beta_4}$ or $\varepsilon_{\boldsymbol{\beta}}^{\max} = \overline{\varepsilon}_{\beta_1} \times \underline{\varepsilon}_{\beta_2} \times \varepsilon_{\beta_3} \times \overline{\varepsilon}_{\beta_4}$. The new solution spaces are composed of only the third dimension. $\boldsymbol{\xi}_{\boldsymbol{\beta}}^{\min}$ and $\boldsymbol{\xi}_{\boldsymbol{\beta}}^{\max}$ are given by $\boldsymbol{\xi}_{\boldsymbol{\beta}}^{\min} = [\underline{\varepsilon}_{\beta_1}, \overline{\varepsilon}_{\beta_2}, \xi_{\beta_3}, \underline{\varepsilon}_{\beta_4}]$ and $\boldsymbol{\xi}_{\boldsymbol{\beta}}^{\max} = [\overline{\varepsilon}_{\beta_1}, \underline{\varepsilon}_{\beta_2}, \xi_{\beta_3}, \overline{\varepsilon}_{\beta_4}]$, respectively. In addition, we can find $\boldsymbol{\xi}_{\boldsymbol{\beta}_{p1}} = \overline{\varepsilon}_{\beta_2}$, $\boldsymbol{\xi}_{\boldsymbol{\beta}_{p2}} = [\underline{\varepsilon}_{\beta_1}, \underline{\varepsilon}_{\beta_4}]$, and $\boldsymbol{\xi}_{\boldsymbol{\beta}_{p3}} = \xi_{\beta_3}$. Thus, $\boldsymbol{\xi}_{\boldsymbol{\beta}_{p1}}$ and $\boldsymbol{\xi}_{\boldsymbol{\beta}_{p2}}$ contain all constants, and $\boldsymbol{\xi}_{\boldsymbol{\beta}_{p3}}$ contains all unknown evidence variables, implying $\psi_{\boldsymbol{\alpha}_{p1}}(\boldsymbol{\xi}_{\boldsymbol{\beta}_{p1}})$ and $\psi_{\boldsymbol{\alpha}_{p2}}(\boldsymbol{\xi}_{\boldsymbol{\beta}_{p2}})$ as constants, and $\psi_{\boldsymbol{\alpha}_{p3}}(\boldsymbol{\xi}_{\boldsymbol{\beta}_{p3}})$ as the part that should be solved iteratively. This example intuitively illustrates the reduction in solution space.

The reduction in solution space depends on the number of monotonic dimensions of the surrogate model. If $r_3 = d$, the SSR-ETM is transformed into ETM, implying that the solution space cannot be reduced. In this case, the SSR-ETM takes additional time for monotonicity analysis, which is also the limitation of the SSR-ETM. Nevertheless, the

SSR-ETM effectively narrows the size of the solution space from d to r_3 as long as $r_3 < d$. Moreover, the solution space is reduced to a point when $r_3 = 0$.

3.5. Evidence-Theory-Based Response Analysis Using the Solution Space Reduction Technique

The extremum of the system response in each joint focal element should be determined for evidence-theory-based UQ. Suppose the monotonicity of the surrogate model determined by PSO is accurate, then, based on the inference in Section 3.4 and the solution space reduction technique, the optimisation problem in Equation (26) is exactly equivalent to

$$\underline{C}(\boldsymbol{\xi}_{\boldsymbol{\beta}})/\overline{C}(\boldsymbol{\xi}_{\boldsymbol{\beta}}) = \min/\max \begin{cases} \sum\limits_{\boldsymbol{\alpha}\in\tilde{\boldsymbol{\lambda}}_{\min}} f_{\boldsymbol{\alpha}}\psi_{\boldsymbol{\alpha}}(\xi_{\boldsymbol{\beta}}),\ r_3 = d \\ \sum\limits_{\boldsymbol{\alpha}\in\tilde{\boldsymbol{\lambda}}_{\min}} f_{\alpha}\psi_{\boldsymbol{\alpha}_{p1}}(\boldsymbol{\xi}_{\boldsymbol{\beta}_{p1}})\psi_{\boldsymbol{\alpha}_{p2}}(\boldsymbol{\xi}_{\boldsymbol{\beta}_{p2}})\psi_{\boldsymbol{\alpha}_{p3}}(\boldsymbol{\xi}_{\boldsymbol{\beta}_{p3}}),\ 0 < r_3 < d \\ \sum\limits_{\boldsymbol{\alpha}\in\tilde{\boldsymbol{\lambda}}_{\min}} f_{\alpha}\psi_{\boldsymbol{\alpha}_{p1}}(\boldsymbol{\xi}_{\boldsymbol{\beta}_{p1}})\psi_{\boldsymbol{\alpha}_{p2}}(\boldsymbol{\xi}_{\boldsymbol{\beta}_{p2}})\ r_3 = 0 \end{cases} \tag{38}$$
$$s.t. \boldsymbol{\xi}_{\boldsymbol{\beta}} \in \varepsilon_{\boldsymbol{\beta}}, \boldsymbol{\beta} \in \boldsymbol{k}$$

This optimisation problem can be solved using PSO. Compared with Equation (26), the surrogate model in Equation (38) is divided into three parts according to monotonicity. On the premise that the monotonicity judgment is correct, the theoretical results of these two equations are exactly the same, indicating the same calculation accuracy of the SSR-ETM and ETM. Considering the randomness of PSO and the change in solution space, there may be a slight deviation between the calculation results of these two methods. To sum up, the SSR-ETM relies on the solution space reduction technique to improve computational efficiency by reducing the solution space in extremum analysis, and the computational accuracy is almost the same as that of the ETM.

After calculating $\underline{C}(\boldsymbol{\xi}_{\boldsymbol{\beta}})$ and $\overline{C}(\boldsymbol{\xi}_{\boldsymbol{\beta}})$, four indicators can be rewritten as

$$\mathrm{CBF}(u) = \sum_{\{\varepsilon_{\boldsymbol{\beta}} | \overline{C}(\boldsymbol{\xi}_{\boldsymbol{\beta}}) \le u, \boldsymbol{\beta}\in\boldsymbol{\kappa}\}} m(\varepsilon_{\boldsymbol{\beta}}), \tag{39}$$

$$\mathrm{CPF}(u) = \sum_{\{\varepsilon_{\boldsymbol{\beta}} | \underline{C}(\boldsymbol{\xi}_{\boldsymbol{\beta}}) \le u, \boldsymbol{\beta}\in\boldsymbol{\kappa}\}} m(\varepsilon_{\boldsymbol{\beta}}), \tag{40}$$

$$\mu^{\mathrm{I}} = \sum_{\boldsymbol{\beta}\in\boldsymbol{\kappa}} C^{\mathrm{I}}(\boldsymbol{\xi}_{\boldsymbol{\beta}}) m(\varepsilon_{\boldsymbol{\beta}}), \tag{41}$$

$$\mathrm{var}^{\mathrm{I}} = \sum_{\boldsymbol{\beta}\in\boldsymbol{\kappa}} \left(C^{\mathrm{I}}(\boldsymbol{\xi}_{\boldsymbol{\beta}}) - \mu^{\mathrm{I}}\right)^2 m(\varepsilon_{\boldsymbol{\beta}}), \tag{42}$$

where $C^{\mathrm{I}}(\boldsymbol{\xi}_{\boldsymbol{\beta}}) = \left[\underline{C}(\boldsymbol{\xi}_{\boldsymbol{\beta}}), \overline{C}(\boldsymbol{\xi}_{\boldsymbol{\beta}})\right]$.

Algorithm 2 shows the pseudo-code of the SSR-ETM. In Algorithm 2, $\psi_{\boldsymbol{\alpha}_{\mathbf{p1}}}(\boldsymbol{\xi}_{\boldsymbol{\beta}_{\mathbf{p1}}})$ and $\psi_{\boldsymbol{\alpha}_{\mathbf{p2}}}(\boldsymbol{\xi}_{\boldsymbol{\beta}_{\mathbf{p2}}})$ remain unchanged in the entire loop, and the value of $\psi_{\boldsymbol{\alpha}_{\mathbf{p3}}}(\boldsymbol{\xi}_{\boldsymbol{\beta}_{\mathbf{p3}}})$ depends on $\boldsymbol{\xi}_{\boldsymbol{\beta}_{\mathbf{p3}}}$ generated by PSO.

Essentially, both the SSR-ETM and ETM use PSO to calculate the extremum of the surrogate model $2N_f$ times. The difference is that the particle dimension of PSO in the SSR-ETM is r_3, while the particle dimension in the ETM is d. Therefore, when N_f is relatively large and $r_3 < d$, the computational cost of the SSR-ETM for monotonicity analysis is relatively small, thus it is more efficient than the ETM.

Algorithm 2 Solution-space-reduction-based evidence theory method (SSR-ETM)

Input: Monotonicity of the surrogate model determined by Algorithm 1, joint focal elements (solution spaces) ε_{β}, and BPAs $m(\varepsilon_{\beta})$, $\boldsymbol{\beta} \in \boldsymbol{\kappa}$.
1. **For** $\boldsymbol{\beta} \in \boldsymbol{\kappa}$
2. **If** $r_3 < d$
3. Use Equation (37) to generate $\boldsymbol{\xi}_{\boldsymbol{\beta}_{\mathrm{p1}}}$ and $\boldsymbol{\xi}_{\boldsymbol{\beta}_{\mathrm{p2}}}$
4. Use Equation (16) to calculate $\psi_{\boldsymbol{\alpha}_{\mathrm{p1}}}(\boldsymbol{\xi}_{\boldsymbol{\beta}_{\mathrm{p1}}})$ and $\psi_{\boldsymbol{\alpha}_{\mathrm{p2}}}(\boldsymbol{\xi}_{\boldsymbol{\beta}_{\mathrm{p2}}})$.
5. **End**
6. **While** PSO has not searched the extremum of $C(\boldsymbol{\xi}_{\boldsymbol{\beta}})$ **and** $r_3 > 0$
7. Use PSO to generate $\boldsymbol{\xi}_{\boldsymbol{\beta}_{\mathrm{p3}}}$.
8. Calculate $\psi_{\boldsymbol{\alpha}_{\mathrm{p3}}}(\boldsymbol{\xi}_{\boldsymbol{\beta}_{\mathrm{p3}}})$ using Equation (16).
9. Calculate $C(\boldsymbol{\xi}_{\boldsymbol{\beta}})$.
10. **End**
11. Store $\underline{C}(\boldsymbol{\xi}_{\boldsymbol{\beta}})/\overline{C}(\boldsymbol{\xi}_{\boldsymbol{\beta}})$.
12. **End**
13. Calculate the four indicators using Equations (39)–(42).

Output: CBF, CPF, μ^{I}, and $\mathrm{var}^{\mathrm{I}}$.

4. Numerical Examples

In this section, four simple functions and an air spring system with epistemic uncertainty are used to compare the SSR-ETM and the ETM. The differences between the two methods are discussed in Section 3. The results were acquired using MATLAB R2021b on a 3.70 GHz AMD Ryzen Threadripper 3970X 32-Core CPU. The PSO used the built-in function "Particleswarm" of MATLAB, and all other parameters were default values, except for keeping the "Vectorized" on. The modified "leave-one-out" error ε was used as the error metrics; more details can be found in [51]. We also used some open-source code from UQLab [58]. The necessary parameters will be illustrated in each numerical example.

4.1. Simple Functions

Let us consider the following function:

$$y(\boldsymbol{\xi}) = I_m \sum_{i=\min\{1,m\}}^{m} (\xi_i + 2)^4 + I_n \sum_{j=\min\{1,n\}}^{n} (\xi_j - 0.5)^4, \tag{43}$$

where $\xi_i, \xi_j \in [-1, 1]$ are independent evidence variables; I_m and I_n are defined as

$$I_m = \begin{cases} 0, m = 0 \\ \frac{1}{m}, m \neq 0 \end{cases}, I_n = \begin{cases} 0, n = 0 \\ \frac{1}{n}, n \neq 0 \end{cases}. \tag{44}$$

The partial derivative of the above function is given as

$$\frac{\partial y}{\partial \xi_l} = \begin{cases} \frac{4(\xi_l+2)^3}{m}, l = i > 0 \\ \frac{4(\xi_l-0.5)^3}{n}, l = j > 0 \end{cases}. \tag{45}$$

Thus, the function is monotonic in m dimensions and non-monotonic in n dimensions. Four functions derived from the function in Equation (43) are designed to illustrate the superiority of the SSR-ETM. In these four functions, N_{BPA} focal elements with the same BPAs are allocated to each evidence variable. For example, the focal elements of an evidence variable in $N_{\mathrm{BPA}} = 2$ are set to [−1,0] and [0,1], with BPAs of 50% and 50%, respectively. Information on the four functions is presented in Table 1. In the simple functions, the number of samples was $N = 60(m + n)$, the "leave-one-out" error was $\varepsilon = 1 \times 10^{-20}$, and the highest order of the polynomial was eight. We set ε so small because there are many items in the candidate base for high-dimensional functions. In practical engineering problems, $10^{-4} \sim 10^{-3}$ is appropriate because PCE usually contains very few lower order terms.

Table 1. Information on the four functions.

Function	Values of m and n	N_{BPA}
Non-monotonic function	$m = 0,\ n = 1, 2, \ldots, 20$	2
Monotonic function	$m = 1, 2, \ldots, 20,\ n = 0$	2
15-dimensional function	$m + n = 15,\ m \geq 0, n \geq 0$	2
5-dimensional function	$m + n = 5,\ m \geq 1, n \geq 0$	2, 3, ..., 8

The results showed that the four indicators about these simple functions obtained by the two methods are almost identical to the analytical solutions, indicating the high computational accuracy of the two methods. Because the plotted curves are almost coincident (similar to Figures 8 and 9) and limited by the fact that CPF and CBF are not suitable for drawing in the form of relative error, these indicators of simple functions are not exhibited here to improve readability and to emphasize the advantages of the SSR-ETM in terms of computational efficiency.

4.1.1. Non-Monotonic Function

The non-monotonic function shown in Equation (46) was used to study the performance of the SSR-ETM when all dimensions are non-monotonic. In this case, the SSR-ETM transforms into the ETM. This implies that the solution space remains unchanged.

$$y(\boldsymbol{\xi}) = \frac{1}{n}\sum_{i=1}^{n}(\xi_i - 0.5)^4, n = 1, 2, \ldots, 20 \tag{46}$$

As depicted in Figure 3, the SSR-ETM requires additional time for monotonicity analysis and solution space reduction, yet it is entirely acceptable. The SSR-ETM takes only approximately 0.54 s longer than the ETM when the number of non-monotonic dimensions is 20. Therefore, the SSR-ETM features a low-risk cost. In addition, the computation time of both methods rapidly increased with the number of dimensions. This is the limitation of the ETM in dealing with high-dimensional uncertainty problems. The performance of the SSR-ETM is not optimistic in this special case, either. However, it should be pointed out that such a special case rarely occurs in high-dimensional engineering problems.

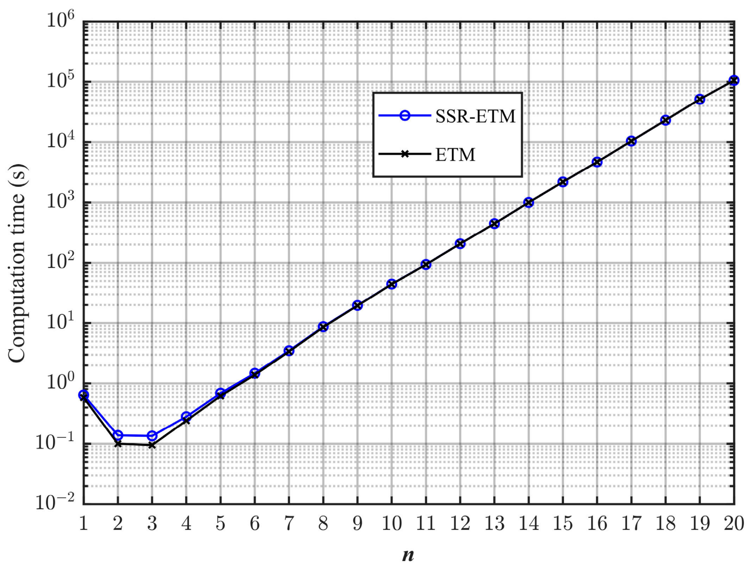

Figure 3. Computation time of the two methods for the non-monotonic function.

4.1.2. Monotonic Function

To assess the performance of the SSR-ETM under the assumption that all dimensions are monotonic, a monotonic function was designed as follows:

$$y(\boldsymbol{\xi}) = \frac{1}{m}\sum_{i=1}^{m}(\xi_i + 2)^4, m = 1, 2, \ldots, 20 \tag{47}$$

In this case, the SSR-ETM precisely locates the minimum and maximum points via monotonicity analysis. Accordingly, we can see from Figure 4 that the efficiency of the SSR-ETM is drastically improved compared with that of the ETM when m assumes a large value. Although the SSR-ETM requires additional time for monotonicity analysis and solution space reduction, it is still faster than the ETM. The SSR-ETM requires no more than 580 s to deal with the uncertainty problem containing 2^{20} joint focal elements, while the ETM requires more than 90,000 s. Moreover, the SSR-ETM remains powerful despite the increase in monotonic dimension, while the computation time of the ETM grows explosively. Because of the short calculation time required for UQ, a small turn appeared around $m = 3$.

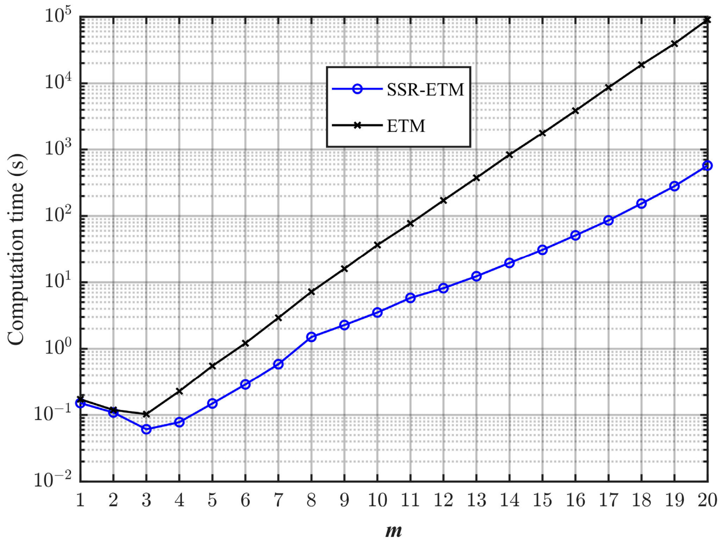

Figure 4. Computation time of the two methods for the monotonic function.

4.1.3. Fifteen-Dimensional Function

Equation (48) expresses the 15-dimensional function designed to investigate the influence of the number of monotonic dimensions on computing efficiency.

$$y(\boldsymbol{\xi}) = I_m \sum_{i=I_m}^{m}(\xi_i + 2)^4 + I_n \sum_{j=I_n}^{n}(\xi_j - 0.5)^4, m + n = 15, m \geq 0, n \geq 0 \tag{48}$$

As shown in Figure 5, the computation time of the SSR-ETM is notably shortened as the number of monotonic dimensions increases, owing to the reduction in the solution space. In contrast, the computation time of ETM fluctuates within a certain range. The SSR-ETM can save approximately 2175 s for a completely monotonic function compared with a completely non-monotonic function; this comparison result is valid only for a function with a dimension of 15 and a number of joint focal elements of 2^{15}. Thus, the efficiency improvement realized by solution space reduction is significant. Although the time invested in monotonicity analysis and solution space reduction may add additional time overall, it is worthwhile.

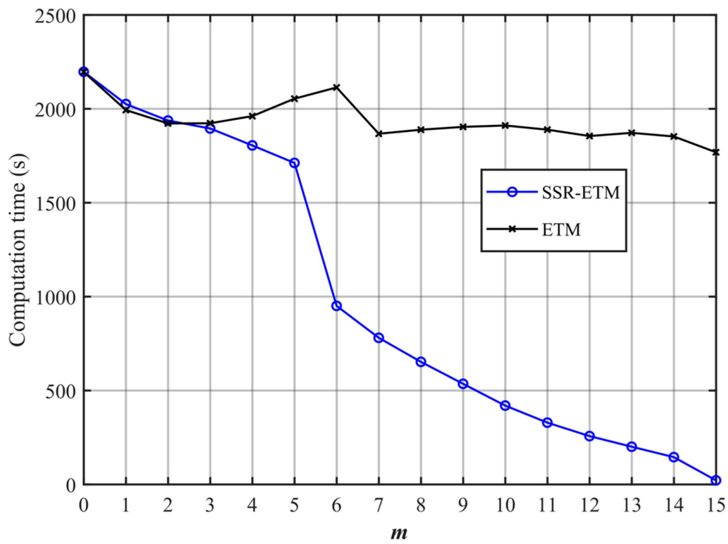

Figure 5. Computation time of the two methods for the 15-dimensional function.

4.1.4. Five-Dimensional Function

Equation (49) expresses the five-dimensional function designed to illustrate the impact of the number of joint focal elements on the computational efficiency advantage of the SSR-ETM.

$$y(\boldsymbol{\xi}) = I_m \sum_{i=\min\{1,m\}}^{m} (\xi_i + 2)^4 + I_n \sum_{j=\min\{1,n\}}^{n} (\xi_j - 0.5)^4, m + n = 5,\ m \geq 1, n \geq 0 \quad (49)$$

Figure 6 reports the computation time ratio of the SSR-ETM to the ETM for different m and N_{BPA}. This illustrates that the computation time ratio of the two methods tends to be stable when the number of joint focal elements reaches a certain degree, implying that the efficiency advantage of the SSR-ETM is mainly affected by the number of monotonic dimensions rather than the number of joint focal elements. Owing to the stability of the SSR-ETM, it is suitable for dealing with epistemic uncertainty problems with numerous joint focal elements.

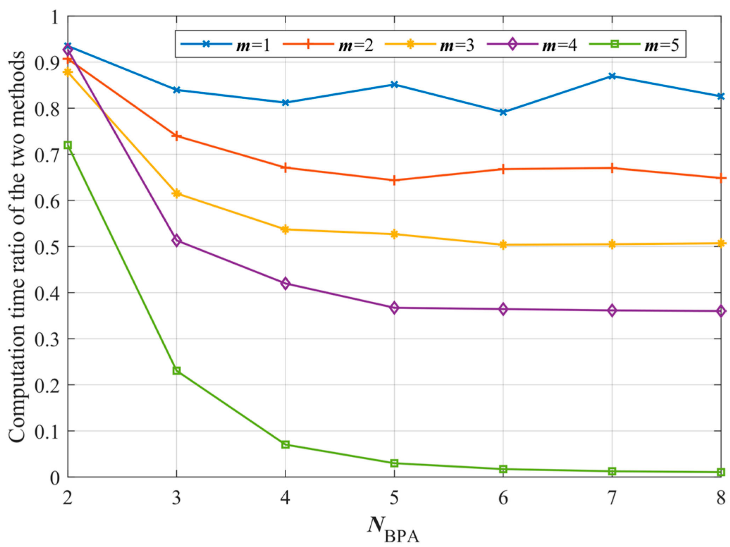

Figure 6. Computation time ratio of the SSR-ETM to the ETM for the five-dimensional function.

4.1.5. Summary of the Results of the Four Simple Functions

The results obtained for the above four simple functions support the following conclusions.

(i) The SSR-ETM features high computational accuracy that is almost the same as that of the ETM because it only divides the surrogate model into monotonic and non-monotonic parts.
(ii) Although the SSR-ETM requires a minuscule amount of time for monotonicity analysis and solution space reduction, it may render remarkable benefits, specifically when the surrogate model is monotonic in all dimensions. When the surrogate model is non-monotonic in all dimensions, the SSR-ETM maintains almost the same computing efficiency as the ETM.
(iii) The SSR-ETM performs better when there are more monotonic dimensions.
(iv) The number of joint focal elements exhibits a negligible effect on the calculation efficiency advantage of the SSR-ETM over the ETM when it reaches a certain degree.

4.2. Air Spring System with Epistemic Uncertainty

4.2.1. Finite Element Model (FEM) of an Air Spring System

Figure 7 shows the air spring finite element model (FEM). The air spring system comprises an upper cover, lower seat, capsule, and cord layers. A total of 119,360 elements were used in modelling, including 30,960 C3D8H elements for the capsule, 35,360 C3D8R elements for the upper cover and lower seat, 49,360 SFM3D4R elements for the cord layer modelled by the rebar layer, and 80 C3D6H elements and 3600 C3D6 elements for the junction between the upper cover and the capsule. The capsule is made of a hyper-elastic material whose constitutive relation is characterised by the Mooney–Rivlin model [59,60].

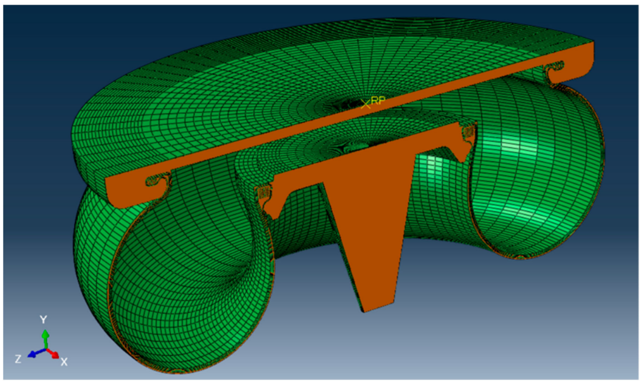

Figure 7. FEM of an air spring.

4.2.2. Air Springs with Uncertain Parameters

Air springs are involved in these uncertainties. The uncertain vector $\boldsymbol{Z}$, which is composed of five uncertain parameters of air springs that are assumed to be independent, is expressed as follows:

$$\boldsymbol{Z} = [E, \varphi, l, S, \delta]^{\mathrm{T}}, \tag{50}$$

where E, φ, l, and S are the Young's modulus, angle, spacing, and cross-sectional area of the cords, respectively, and δ is the thickness of the capsule. The evidence theory model defines these uncertain parameters as evidence variables, whose focal elements and corresponding BPAs are listed in Table 2. The system response K, the vertical static stiffness of air springs, can be obtained by solving the following finite element equation:

$$K = M(\boldsymbol{Z}). \tag{51}$$

Table 2. Information about the air spring system.

E (MPa)		φ (Degree)		l (mm)		S (mm^2)		δ (mm)	
Focal Element	**BPA (%)**	**Focal Element**	**BPA (%)**	**Focal Element**	**BPA (%)**	**Focal Element**	**BPA (%)**	**Focal Element**	**BPA (%)**
[1657,1675]	3.90	[40.8,41.5]	0.85	[1.40,1.42]	5.05	[5.4,5.5]	0.47	[6.0,6.2]	0.65
[1675,1700]	7.64	[41.5,42.0]	1.07	[1.42,1.44]	7.28	[5.5,5.6]	0.99	[6.2,6.4]	2.12
[1700,1725]	7.11	[42.0,42.5]	3.06	[1.44,1.46]	8.33	[5.6,5.7]	4.74	[6.4,6.6]	25.36
[1725,1750]	5.62	[42.5,43.0]	4.13	[1.46,1.48]	17.95	[5.7,5.8]	9.67	[6.6,6.8]	20.36
[1750,1775]	7.28	[43.0,43.5]	5.11	[1.48,1.50]	14.63	[5.8,5.9]	20.97	[6.8,7.0]	21.21
[1775,1800]	7.67	[43.5,44.0]	9.67	[1.50,1.52]	19.51	[5.9,6.0]	25.98	[7.0,7.2]	18.54
[1800,1825]	7.78	[44.0,44.5]	8.75	[1.52,1.54]	11.46	[6.0,6.1]	20.86	[7.2,7.4]	5.10
[1825,1850]	9.04	[44.5,45.0]	14.68	[1.54,1.56]	8.40	[6.1,6.2]	9.62	[7.4,7.6]	4.33
[1850,1875]	7.25	[45.0,45.5]	12.61	[1.56,1.58]	5.98	[6.2,6.3]	4.95	[7.6,7.8]	1.98
[1875,1900]	5.38	[45.5,46.0]	8.92	[1.58,1.60]	1.41	[6.3,6.4]	1.33	[7.8,8.0]	0.35
[1900,1925]	7.47	[46.0,46.5]	7.61			[6.4,6.5]	0.42		
[1925,1950]	7.69	[46.5,47.0]	7.05						
[1950,1975]	7.82	[47.0,47.5]	9.11						
[1975,1996]	8.35	[47.5,48.0]	4.62						
		[48.0,48.5]	1.73						
		[48.5,49.1]	1.03						

4.2.3. SSR-ETM for Stiffness Evaluation

For a given ED $\boldsymbol{X} = \left\{\boldsymbol{Z}^{(1)}, \ldots, \boldsymbol{Z}^{(N)}\right\}^{\mathrm{T}}$ and its corresponding model evaluations $\boldsymbol{Y} = \left\{K^{(1)}, \ldots, K^{(N)}\right\}^{\mathrm{T}}$, one can use the two methods to calculate the bounds of expectation and variance of the vertical static stiffness at different initial pressures. CBF and CPF at different initial pressures are also available. Owing to fewer uncertain variables of the air spring system, we incorporated 10^5 random samples and the vertex method [61] to obtain the extremum in each joint focal element and the reference solutions of the four indicators. Note that the reference solutions were obtained based on the surrogate model rather than the computational model or FEM. In this numerical example, the number of samples was 200, the "leave-one-out" error was 1×10^{-3}, and the highest order of the polynomial was 12. The results of the stiffness evaluation are presented in Figures 8–10.

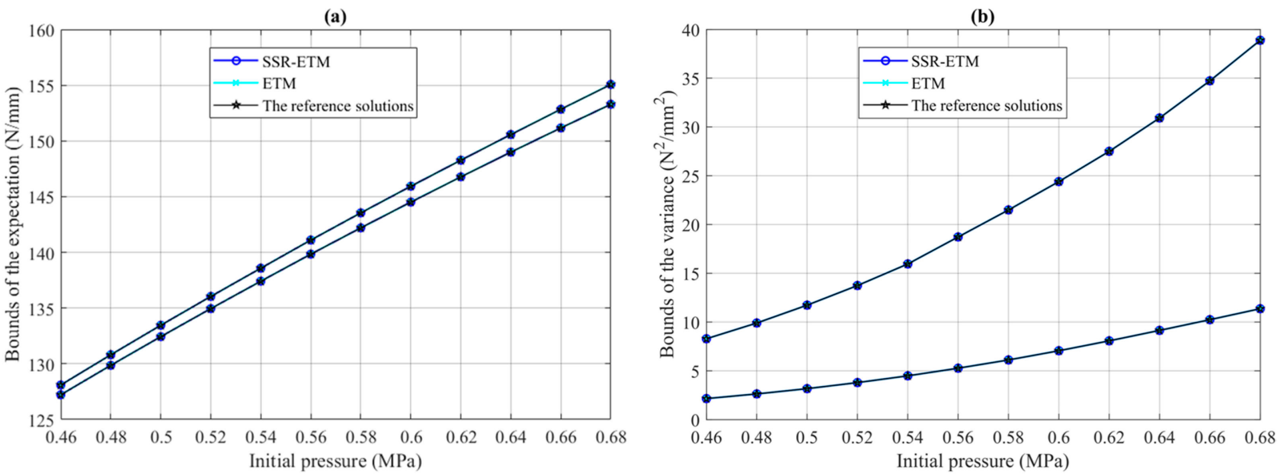

Figure 8. Bounds of the expectation (**a**) and variance (**b**) of the vertical static stiffness and their reference solutions at different initial pressures.

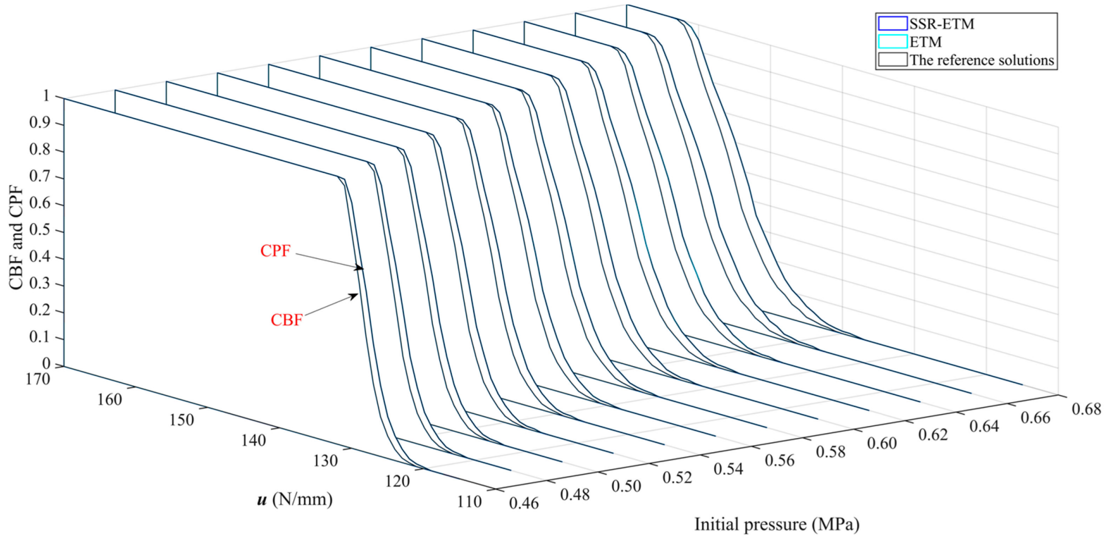

Figure 9. CBF and CPF of the two methods and their reference solutions for the air spring system.

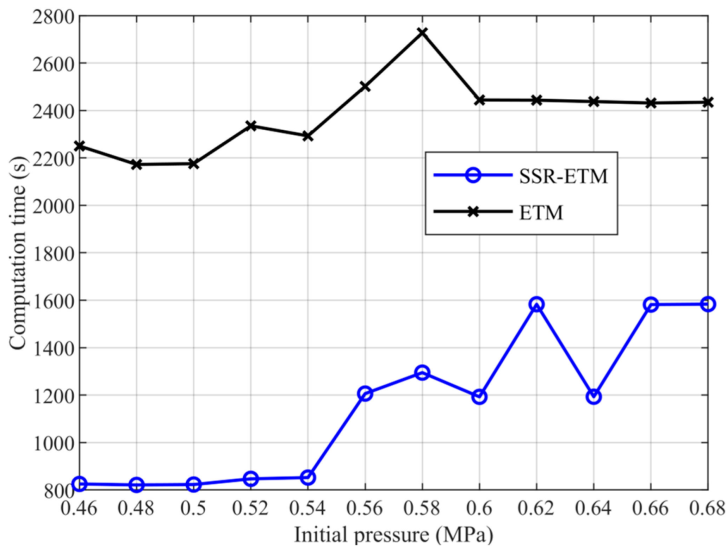

Figure 10. Computation time of the two methods at different initial pressures.

We can observe from Figure 8 that the bounds of the expectation and variance of the vertical static stiffness increase with the initial pressure. This is because the stress on the air springs increases with the initial pressure, leading to a higher vertical static stiffness owing to the adjustable stiffness characteristics.

As depicted in Figure 9, the curves of CPF are close to the CBF. This is because the minimum in each joint focal element is close to that of the maximum. The curves of the four indicators obtained by the two methods are almost coincident with that of the reference solutions, proving both methods provide accurate results of stiffness evaluation at different initial pressures as long as the surrogate model is well established.

Accelerated by the reduction in solution space, the SSR-ETM spends less time than the ETM on UQ (see Figure 10). Particularly, the surrogate model of the air spring system is monotonic in four dimensions when the initial pressure is between 0.46 MPa and 0.54 MPa. The SSR-ETM saves about 1400 s for this uncertain system with only five uncertain variables. The SSR-ETM still performs well under 0.56–0.68 MPa as two or three dimensions are reduced. Thus, the SSR-ETM was proved to be valid.

5. Conclusions

In this study, we propose the SSR-ETM. Initially, SAPCE was used to approximate the computational model. Thereafter, PSO was employed for monotonicity analysis. Based on monotonicity analysis, the solution space can be reduced if the surrogate model is monotonic in at least one dimension. The reduced solution space is conducive to accelerating extremum analysis. Ultimately, four simple functions and an air-spring system with epistemic uncertainty successfully verified the validity of the SSR-ETM. Our results support the following conclusions:

(i) The SSR-ETM demonstrates a high computing accuracy almost comparable to that of the ETM as long as the surrogate model is well established.
(ii) Compared with the ETM, the SSR-ETM adds minimal additional time for monotonicity analysis and solution space reduction.
(iii) More monotonic dimensions contribute to a higher efficiency advantage of the SSR-ETM. In particular, when all dimensions are monotone, the SSR-ETM exhibits a significant efficiency advantage over the ETM.
(iv) The SSR-ETM performed better than the ETM in the stiffness evaluation of the air springs with epistemic uncertainty.

In conclusion, the SSR-ETM is a promising UQ method with low risk and high return, particularly suitable for engineering applications with prominent monotonicity. However, the SSR-ETM still does not perform well for the high-dimensional surrogate model without any monotonic dimension or with few monotonic dimensions. In addition, it requires very high accuracy of the surrogate model. Moreover, the number of extremum analyses in SSR-ETM multiplies with the number of focal elements contained in the number of uncertain variables. Although we have listed several numerical examples with 2^{20} joint focal elements, the number of extremum analyses in SSR-ETM is the product of the number of focal elements in all variables, which makes it difficult for the SSR-ETM to deal with problems with many uncertainty variables. In future work, it is necessary to study further how to solve these problems.

Author Contributions: Conceptualization, S.Y. and K.J.; methodology, S.Y.; software, K.J.; validation, S.Y. and K.J.; formal analysis, K.J.; investigation, Y.B.; resources, S.Y., W.Z. and Z.W.; data curation, K.J. and Y.B.; writing—original draft preparation, K.J.; writing—review and editing, K.J.; visualization, K.J.; supervision, S.Y.; project administration, S.Y., W.Z. and Z.W. All authors have read and agreed to the published version of the manuscript.

Funding: This research received no external funding.

Data Availability Statement: Please send an email to jinkeliang@csu.edu.cn if any questions about the code associated with this article. The air spring model is confidential and will not be available.

Conflicts of Interest: The authors declare no conflict of interest.

References

1. Chen, J.-J.; Yin, Z.-H.; Yuan, X.-J.; Qiu, G.-Q.; Guo, K.-H.; Wang, X.-L. A refined stiffness model of rolling lobe air spring with structural parameters and the stiffness characteristics of rubber bellows. *Measurement* **2021**, *169*, 108355. [CrossRef]
2. Chen, J.-J.; Yin, Z.-H.; Rakheja, S.; He, J.-H.; Guo, K.-H. Theoretical modelling and experimental analysis of the vertical stiffness of a convoluted air spring including the effect of the stiffness of the bellows. *Proc. Inst. Mech. Eng. Part D J. Automob. Eng.* **2018**, *232*, 547–561. [CrossRef]
3. Hora, S.C. Aleatory and epistemic uncertainty in probability elicitation with an example from hazardous waste management. *Reliab. Eng. Syst. Saf.* **1996**, *54*, 217–223. [CrossRef]
4. Hüllermeier, E.; Waegeman, W. Aleatoric and epistemic uncertainty in machine learning: An introduction to concepts and methods. *Mach. Learn.* **2021**, *110*, 457–506. [CrossRef]
5. Salehi, S.; Raisee, M.; Cervantes, M.J.; Nourbakhsh, A. An efficient multifidelity $\ell 1$-minimization method for sparse polynomial chaos. *Comput. Methods Appl. Mech. Eng.* **2018**, *334*, 183–207. [CrossRef]
6. Tarakanov, A.; Elsheikh, A.H. Regression-based sparse polynomial chaos for uncertainty quantification of subsurface flow models. *J. Comput. Phys.* **2019**, *399*, 108909. [CrossRef]

7. Thapa, M.; Mulani, S.B.; Walters, R.W. A new non-intrusive polynomial chaos using higher order sensitivities. *Comput. Methods Appl. Mech. Eng.* **2018**, *328*, 594–611. [CrossRef]
8. Torre, E.; Marelli, S.; Embrechts, P.; Sudret, B. Data-driven polynomial chaos expansion for machine learning regression. *J. Comput. Phys.* **2019**, *388*, 601–623. [CrossRef]
9. Yin, S.; Yu, D.; Luo, Z.; Xia, B. An arbitrary polynomial chaos expansion approach for response analysis of acoustic systems with epistemic uncertainty. *Comput. Methods Appl. Mech. Eng.* **2018**, *332*, 280–302. [CrossRef]
10. Yin, S.; Yu, D.; Yin, H.; Lü, H.; Xia, B. Hybrid evidence theory-based finite element/statistical energy analysis method for mid-frequency analysis of built-up systems with epistemic uncertainties. *Mech. Syst. Signal Process.* **2017**, *93*, 204–224. [CrossRef]
11. Yin, S.; Yu, D.; Ma, Z.; Xia, B. A unified model approach for probability response analysis of structure-acoustic system with random and epistemic uncertainties. *Mech. Syst. Signal Process.* **2018**, *111*, 509–528. [CrossRef]
12. Pantelides, C.P.; Ganzerli, S. Comparison of fuzzy set and convex model theories in structural design. *Mech. Syst. Signal Process.* **2001**, *15*, 499–511. [CrossRef]
13. Yang, S.; Han, J.; Xia, L.; Chen, Y.-H. An optimal fuzzy-theoretic setting of adaptive robust control design for a lower limb exoskeleton robot system. *Mech. Syst. Signal Process.* **2020**, *141*, 106706. [CrossRef]
14. Huang, F.; Sava, A.; Adjallah, K.H.; Wang, Z. Fuzzy model identification based on mixture distribution analysis for bearings remaining useful life estimation using small training data set. *Mech. Syst. Signal Process.* **2021**, *148*, 107173. [CrossRef]
15. van Mierlo, C.; Burmberger, L.; Daub, M.; Duddeck, F.; Faes, M.G.; Moens, D. Interval methods for lack-of-knowledge uncertainty in crash analysis. *Mech. Syst. Signal Process.* **2022**, *168*, 108574. [CrossRef]
16. Zhang, W.; Liu, J.; Cho, C.; Han, X. A hybrid parameter identification method based on Bayesian approach and interval analysis for uncertain structures. *Mech. Syst. Signal Process.* **2015**, *60*, 853–865. [CrossRef]
17. Deng, Z.; Guo, Z.; Zhang, X. Interval model updating using perturbation method and radial basis function neural networks. *Mech. Syst. Signal Process.* **2017**, *84*, 699–716. [CrossRef]
18. Fang, S.-E.; Zhang, Q.-H.; Ren, W.-X. An interval model updating strategy using interval response surface models. *Mech. Syst. Signal Process.* **2015**, *60*, 909–927. [CrossRef]
19. Zhu, W.; Chen, N.; Liu, J.; Beer, M. A probability-box-based method for propagation of multiple types of epistemic uncertainties and its application on composite structural-acoustic system. *Mech. Syst. Signal Process.* **2021**, *149*, 107184. [CrossRef]
20. Crespo, L.G.; Kenny, S.P.; Giesy, D.P. Reliability analysis of polynomial systems subject to p-box uncertainties. *Mech. Syst. Signal Process.* **2013**, *37*, 121–136. [CrossRef]
21. Su, X.; Mahadevan, S.; Xu, P.; Deng, Y. Dependence Assessment in Human Reliability Analysis Using Evidence Theory and AHP. *Risk Anal.* **2015**, *35*, 1296–1316. [CrossRef] [PubMed]
22. Zhang, Z.; Jiang, C.; Wang, G.G.; Han, X. First and second order approximate reliability analysis methods using evidence theory. *Reliab. Eng. Syst. Saf.* **2015**, *137*, 40–49. [CrossRef]
23. Shamlou, A.; Reza Feyzi, M.; Behjat, V. Interpretation of frequency response analysis of power transformer based on evidence theory. *IET Gener. Transm. Distrib.* **2019**, *13*, 3879–3887. [CrossRef]
24. Amini, A.; Abdollahi, A.; Hariri-Ardebili, M.A.; Lall, U. Copula-based reliability and sensitivity analysis of aging dams: Adaptive Kriging and polynomial chaos Kriging methods. *Appl. Soft Comput.* **2021**, *109*, 107524. [CrossRef]
25. Hariri-Ardebili, M.A.; Mahdavi, G.; Abdollahi, A.; Amini, A. An RF-PCE hybrid surrogate model for sensitivity analysis of dams. *Water* **2021**, *13*, 302. [CrossRef]
26. Hariri-Ardebili, M.A.; Sudret, B. Polynomial chaos expansion for uncertainty quantification of dam engineering problems. *Eng. Struct.* **2020**, *203*, 109631. [CrossRef]
27. Li, Y.; Hariri-Ardebili, M.A.; Deng, T.; Wei, Q.; Cao, M. A surrogate-assisted stochastic optimization inversion algorithm: Parameter identification of dams. *Adv. Eng. Inform.* **2023**, *55*, 101853. [CrossRef]
28. Shah, H.R.; Hosder, S.; Winter, T. Quantification of Margins and Mixed Uncertainties Using Evidence Theory and Stochastic Expansions. In Proceedings of the 16th AIAA Non-Deterministic Approaches Conference, National Harbor, MD, USA, 13–17 January 2014.
29. Yin, S.; Yu, D.; Yin, H.; Xia, B. A new evidence-theory-based method for response analysis of acoustic system with epistemic uncertainty by using Jacobi expansion. *Comput. Methods Appl. Mech. Eng.* **2017**, *322*, 419–440. [CrossRef]
30. Zhang, J.; Gong, W.; Yue, X.; Shi, M.; Chen, L. Efficient reliability analysis using prediction-oriented active sparse polynomial chaos expansion. *Reliab. Eng. Syst. Saf.* **2022**, *228*, 108749. [CrossRef]
31. Zhang, B.-Y.; Ni, Y.-Q. A hybrid sequential sampling strategy for sparse polynomial chaos expansion based on compressive sampling and Bayesian experimental design. *Comput. Methods Appl. Mech. Eng.* **2021**, *386*, 114130. [CrossRef]
32. Zhang, J.; Yue, X.; Qiu, J.; Zhuo, L.; Zhu, J. Sparse polynomial chaos expansion based on Bregman-iterative greedy coordinate descent for global sensitivity analysis. *Mech. Syst. Signal Process.* **2021**, *157*, 107727. [CrossRef]
33. Zhou, Y.; Lu, Z.; Cheng, K.; Ling, C. An efficient and robust adaptive sampling method for polynomial chaos expansion in sparse Bayesian learning framework. *Comput. Methods Appl. Mech. Eng.* **2019**, *352*, 654–674. [CrossRef]
34. Luthen, N.; Marelli, S.; Sudret, B. Sparse polynomial chaos expansions: Literature survey and benchmark. *SIAM/ASA J. Uncertain. Quantif.* **2021**, *9*, 593–649. [CrossRef]
35. Dempster, A.P. A generalization of Bayesian inference. *J. R. Stat. Soc. Ser. B* **1968**, *30*, 205–232. [CrossRef]
36. Shafer, G. *A Mathematical Theory of Evidence*; Princeton University Press: Princeton, NJ, USA, 1976; Volume 42.

37. Shafer, G.; Pearl, J. *Readings in Uncertain Reasoning*; Morgan Kaufmann Publishers Inc.: Burlington, MA, USA, 1990.
38. Shafer, G. Perspectives on the theory and practice of belief functions. *Int. J. Approx. Reason.* **1990**, *4*, 323–362. [CrossRef]
39. Shafer, G. Dempster-shafer theory. *Encycl. Artif. Intell.* **1992**, *1*, 330–331.
40. Wang, C.; Matthies, H.G. Evidence theory-based reliability optimization design using polynomial chaos expansion. *Comput. Methods Appl. Mech. Eng.* **2018**, *341*, 640–657. [CrossRef]
41. Bai, Y.C.; Jiang, C.; Han, X.; Hu, D.A. Evidence-theory-based structural static and dynamic response analysis under epistemic uncertainties. *Finite Elem. Anal. Des.* **2013**, *68*, 52–62. [CrossRef]
42. Zhou, Y.; Lu, Z.; Cheng, K. Adaboost-based ensemble of polynomial chaos expansion with adaptive sampling. *Comput. Methods Appl. Mech. Eng.* **2022**, *388*, 114238. [CrossRef]
43. Sudret, B. Global sensitivity analysis using polynomial chaos expansions. *Reliab. Eng. Syst. Saf.* **2008**, *93*, 964–979. [CrossRef]
44. Xiu, D.; Karniadakis, G.E. The Wiener–Askey polynomial chaos for stochastic differential equations. *SIAM J. Sci. Comput.* **2002**, *24*, 619–644. [CrossRef]
45. Oladyshkin, S.; Nowak, W. Data-driven uncertainty quantification using the arbitrary polynomial chaos expansion. *Reliab. Eng. Syst. Saf.* **2012**, *106*, 179–190. [CrossRef]
46. Guo, L.; Liu, Y.; Zhou, T. Data-driven polynomial chaos expansions: A weighted least-square approximation. *J. Comput. Phys.* **2019**, *381*, 129–145. [CrossRef]
47. Ahlfeld, R.; Belkouchi, B.; Montomoli, F. SAMBA: Sparse approximation of moment-based arbitrary polynomial chaos. *J. Comput. Phys.* **2016**, *320*, 1–16. [CrossRef]
48. Thapa, M.; Mulani, S.B.; Walters, R.W. Adaptive weighted least-squares polynomial chaos expansion with basis adaptivity and sequential adaptive sampling. *Comput. Methods Appl. Mech. Eng.* **2020**, *360*, 112759. [CrossRef]
49. Fajraoui, N.; Marelli, S.; Sudret, B. Sequential Design of Experiment for Sparse Polynomial Chaos Expansions. *SIAM/ASA J. Uncertain. Quantif.* **2017**, *5*, 1061–1085. [CrossRef]
50. Hosder, S.; Walters, R.; Balch, M. Efficient sampling for non-intrusive polynomial chaos applications with multiple uncertain input variables. In Proceedings of the 48th AIAA/ASME/ASCE/AHS/ASC Structures, Structural Dynamics, and Materials Conference, Honolulu, HI, USA, 23–26 April 2007; p. 1939.
51. Blatman, G.; Sudret, B. Adaptive sparse polynomial chaos expansion based on least angle regression. *J. Comput. Phys.* **2011**, *230*, 2345–2367. [CrossRef]
52. McKay, M.D.; Beckman, R.J.; Conover, W.J. A comparison of three methods for selecting values of input variables in the analysis of output from a computer code. *Technometrics* **2000**, *42*, 55–61. [CrossRef]
53. Kennedy, J.; Eberhart, R. Particle swarm optimization. In *Proceedings of the ICNN'95-International Conference on Neural Networks*; Perth, WA, Australia, 27 November–1 December 1995, pp. 1942–1948.
54. Holland, J.H. *Adaptation in Natural and Artificial Systems: An Introductory Analysis with Applications to Biology, Control, and Artificial Intelligence*; MIT Press: Cambridge, MA, USA, 1992.
55. Dorigo, M.; Birattari, M.; Stutzle, T. Ant colony optimization. *IEEE Comput. Intell. Mag.* **2006**, *1*, 28–39. [CrossRef]
56. Kriz, I.; Pultr, A. *Multivariable Differential Calculus. In Introduction to Mathematical Analysis*; Springer: Basel, Switzerland, 2013; pp. 65–95. [CrossRef]
57. O'Regan, G. Calculus. In *Mathematics in Computing: An Accessible Guide to Historical, Foundational and Application Contexts*; Springer: London, UK, 2013; pp. 247–265. [CrossRef]
58. Marelli, S.; Sudret, B. *UQLab: A Framework for Uncertainty Quantification in Matlab*; American Society of Civil Engineers: Reston, VA, USA, 2014.
59. Mooney, M. A Theory of Large Elastic Deformation. *J. Appl. Phys.* **1940**, *11*, 582–592. [CrossRef]
60. Rivlin, R.S. Large elastic deformations of isotropic materials IV. Further developments of the general theory. *Philos. Trans. R. Soc. London. Ser. A Math. Phys. Sci.* **1948**, *241*, 379–397.
61. Qiu, Z.; Xia, Y.; Yang, J. The static displacement and the stress analysis of structures with bounded uncertainties using the vertex solution theorem. *Comput. Methods Appl. Mech. Eng.* **2007**, *196*, 4965–4984. [CrossRef]